

Received April 3, 2021, accepted April 27, 2021, date of publication May 4, 2021, date of current version May 12, 2021.

Digital Object Identifier 10.1109/ACCESS.2021.3077444

Maximum Energy Capturing Approach for Heaving Wave Energy Converters Using an Estimator-Based Finite Control Set Model Predictive Control

MOHAMMED JAMA¹, BISNI FAHAD MON², ADDY WAHYUDIE²,
AND SAAD MEKHILEF^{3,4}, (Senior Member, IEEE)

¹Emirates Centre of Energy and Environment Research (ECEER), United Arab Emirates University, Al Ain 15551, United Arab Emirates

²Department of Electrical Engineering, United Arab Emirates University, Al Ain 15551, United Arab Emirates

³Power Electronics and Renewable Energy Research Laboratory (PEARL), Department of Electrical Engineering, University of Malaya, Kuala Lumpur 50603, Malaysia

⁴School of Software and Electrical Engineering, Swinburne University of Technology, Melbourne 3000, Australia

Corresponding author: Addy Wahyudie (addy.w@uaeu.ac.ae)

This work was supported in part by the Joint Research Program between UAE University and Asian Universities Alliance (AUA) under Grant 31R169, and in part by the Ph.D. Fund under Grant 31N275.

ABSTRACT The control problem in wave energy continues to remain an open question. This is mainly attributed to the difficulties associated with developing effective, yet economically viable, wave energy-harnessing control strategies, such as resource irregularity, the multidisciplinary nature of the system, and dynamic model uncertainties and ambiguities. Herein, a maximum energy-capturing approach for heaving wave energy converters (WECs) using an estimator-based finite control set model predictive control (FCS-MPC) is proposed. The proposed control strategy utilizes an elaborate nonlinear wave-to-wire model of a heaving WEC. The FCS-MPC is formulated such that a control command trajectory is not required; instead, it searches for the optimum control law—in the form of switching functions—that maximizes the WEC converted electrical energy while imposing soft constraints on the states of the power take-off (PTO) mechanism. Current transducers are deployed to measure the PTO three-phase currents and both mechanical and electrical variables required by the FCS-MPC strategy are estimated using an electrical-based extended Kalman filter (E-EKF). Simulations were performed to assess the effectiveness of the proposed control strategy. Results presented herein clearly show that the proposed referenceless FCS-MPC managed to produce 10%–23% more energy compared with benchmark resistive loading-based techniques with both fixed and variable wave frequency capabilities while utilizing 18%–45% less PTO resources.

INDEX TERMS Wave energy converter, model predictive control, finite control set, extended Kalman filter, permanent magnet linear generator, point absorber, damping control, wave-to-wire model.

LIST OF ABBREVIATIONS

Acronym	Description		
WEC	Wave Energy Converter	PMLG	Permanent Magnet Linear Generator
PTO	Power Take-off	MSC	Machine Side Converter
RL	Resistive Loading	2L-VSC	Two-leg Voltage Source Converter
ACC	Approximate Complex Conjugate	E-EKF	Electrical-based Extended Kalman Filter
AVT	Approximate Optimal Velocity Tracking	RL-FCS-MPC	Referenceless Finite Control Set MPC
MPC	Model Predictive Control	RB-FCS-MPC	Reference-based Finite Control Set MPC
FCS-MPC	Finite Control Set MPC	FLL	Frequency Locked Loop
		SOGI-FLL	Second-order Generalized Integrator FLL
		RMSE	Root Mean Square Error

The associate editor coordinating the review of this manuscript and approving it for publication was S. Ali Arefifar¹.

I. INTRODUCTION

In comparison to solar, wind and hydropower energy sources, marine energy is still largely an untapped source of renewable energy, albeit having a theoretical energy capacity of approximately 77 TW [1]. The main categories of marine energy are wave energy, tidal energy, thermal energy, and osmosis energy [2], [3]. Wave energy—particularly—has continually received increasing worldwide attention for the past two decades. This is mainly attributed to the great potential of this energy resource, which is estimated to be approximately 3.7 TW [4]. Despite its potential, only a fraction of wave energy is believed to be exploitable owing to current technological and economic challenges that hinder the wide-scale development of this promising energy source. The techno-economic viability in wave energy converters (WECs) are mainly influenced by the available wave resource potential, adopted topology of the WEC, effectiveness of the power take-off (PTO) mechanism, and governing control strategy [5]. The WEC control problem is a highly complex problem because WEC comprises multiple interacting systems wherein each system has its own principle of operation and physical limitations. Furthermore, the irregular and intermittent nature of the sea wave resource makes the control problem even harder. Generally, a WEC control strategy should maximize the amount of energy captured from the traveling sea waves, ensuring that different subsystems in the WEC are operating within their physical limitations, and be implementable from the hardware point of view.

Over the years, several classes of control strategies have been proposed in the literature. The basic concept of most of these proposed control strategies is the principle of maximum power transfer or impedance matching. Examples of impedance matching-based control strategies are resistive loading (RL) and approximate complex conjugate (ACC). Despite being easy to implement, these strategies are open-loop, suboptimal, and heavily model-based. Moreover, ACCs often result in unrealistic dynamics (i.e., extreme excursions and control efforts) [6], [7]. Another class of control strategies include servo-tracking based strategies, such as approximate optimal velocity tracking (AVT) with constant excitation force-to-velocity function [8]. Robust variants of the AVT were also reported in [9], [10]. Model predictive control (MPC) strategies also have their own challenges regarding the WEC control problem. Traditional constrained MPC strategies for controlling mechanical dynamics of WECs were proposed in [8], [11]. Parametrized MPC strategies using basis functions were investigated in [12], [13]. Furthermore, heuristic control techniques were deployed to control WECs mainly owing to their lower dependency on the system model, such as fuzzy control [14] and neural networks [15]. Impedance matching control using search algorithms have been proposed in several studies [16], [17].

Herein, a novel referenceless (RL) finite control set MPC (FCS-MPC) strategy for controlling the operation of a heaving WEC is proposed. The control strategy—as the name

implies—does not require online determination of a reference trajectory. Therefore, it is not classified as a servo-control strategy. Instead, it is based on an online constrained optimization problem that needs to be maximized using a search algorithm. The optimization problem cost function calculates the amount of converted electrical energy measured at the terminals of a permanent magnet linear generator (PMLG). FCS-MPC is utilized to obtain an optimum set of switching states—from the possible eight switching states—used to control current flowing in the stator circuit of the machine-side converter (MSC). FCS-MPC is nonlinear; therefore, a nonlinear dynamic model of a WEC can be readily deployed. Both mechanical and electrical models can be combined to form a single predictive control architecture. Furthermore, the FCS-MPC technique is computationally cost-effective, wherein the system states are predicted one sample ahead of the future. Another merit of the proposed control strategy is the use of an electrical-based extended Kalman filter (E-EKF) to estimate WEC states, which include buoy heave displacement, velocity, and wave excitation force. The E-EKF only requires real-time measurement of the PMLG three-phase stator circuitry currents using current transducers. No mechanical sensors are required here, thus enhancing the implementation and reliability of the control strategy. As the adopted predictive control has a one-sample-long prediction horizon, no excitation force forecasting techniques are required. An additional advantage that the FCS-MPC technique contributes is the fact that it does not require any modulation technique because the converter switching states are determined through the online optimization problem prior to applying them directly to the converter switches. The proposed FCS-MPC control strategy produces a unidirectional power flow with relatively low peak-to-average power ratios, therefore PTO systems with low power ratings can be deployed resulting in reducing the development costs of WECs. This paper is organized as follows: Section II discusses the WEC wave-to-wire dynamic model. The proposed control strategies are appropriately derived in Section III. The developed control strategies are analyzed and evaluated via computer simulations in Section IV. Finally, conclusions are drawn in Section V.

II. MODELING OF THE WAVE ENERGY CONVERTER

The WEC under investigation herein is a point absorber with a semispherical buoy that oscillates against a stationary platform, as shown in Fig. 1. The buoy heave motion directly drives a PTO system. In this section, a detailed wave-to-wire nonlinear dynamic model describing the performance of the WEC topology studied herein is derived. The WEC system can be divided into two interacting subsystems. The first subsystem is the PTO subsystem, which converts the mechanical power captured by the WEC buoy into electrical power. Furthermore, the PTO system serves as an actuator in the control system through altering the motion of the WEC buoy in real time. The second subsystem entails the

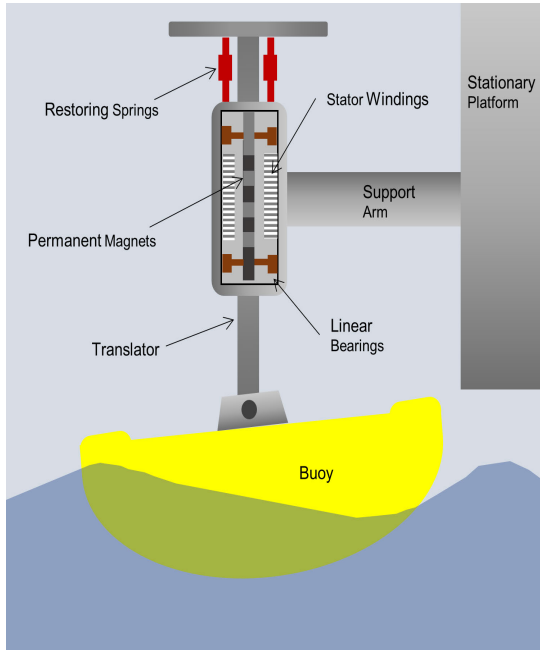


FIGURE 1. Drawing of the heaving WEC system investigated herein.

interaction between the incoming sea waves and the WEC buoy.

A. WEC PTO MODEL

The WEC PTO system comprises a three-phase PMLG and an accompanying three-phase voltage source converter (VSC). The $d-q$ synchronous reference frame model of the PMLG can be expressed as follows [18]:

$$\frac{di_{sd}(t)}{dt} = -\frac{V_{sd}(t)}{L_s} - \frac{R_s}{L_s}i_{sd}(t) + \frac{\pi}{\gamma}v(t)i_{sq}(t), \quad (1)$$

$$\frac{di_{sq}(t)}{dt} = -\frac{V_{sq}(t)}{L_s} - \frac{R_s}{L_s}i_{sq}(t) - \frac{\pi}{\gamma}v(t)i_{sd}(t) - \frac{\pi\psi_{PM}}{\gamma}v(t), \quad (2)$$

where $i_{sd}(t)$, $i_{sq}(t)$, $V_{sd}(t)$, and $V_{sq}(t)$ are the PMLG direct and quadrature stator currents and direct and quadrature stator voltages, respectively. The parameters R_s , L_s , γ , and ψ_{PM} are the stator resistance, stator inductance, armature pole pitch, and flux linkage due to the permanent magnets, respectively. $v(t)$ is the heave velocity of the PMLG translator.

A three-phase two-leg voltage source converter (2L-VSC) is deployed as a MSC to control the PMLG, which consequently controls the motion of the WEC buoy, as shown in Fig. 2. The MSC three-phase voltage vector $V_s(t)$ can be synthesized as function of the three-phase switching function vector $S(t)$ and DC-link voltage V_{dc} [19],

$$\underbrace{\begin{bmatrix} V_{sa}(t) \\ V_{sb}(t) \\ V_{sc}(t) \end{bmatrix}}_{V_s(t)} = \frac{V_{dc}}{3} \underbrace{\begin{bmatrix} 2 & -1 & -1 \\ -1 & 2 & -1 \\ -1 & -1 & 2 \end{bmatrix}}_{K_s} \underbrace{\begin{bmatrix} S_a(t) \\ S_b(t) \\ S_c(t) \end{bmatrix}}_{S(t)}, \quad (3)$$

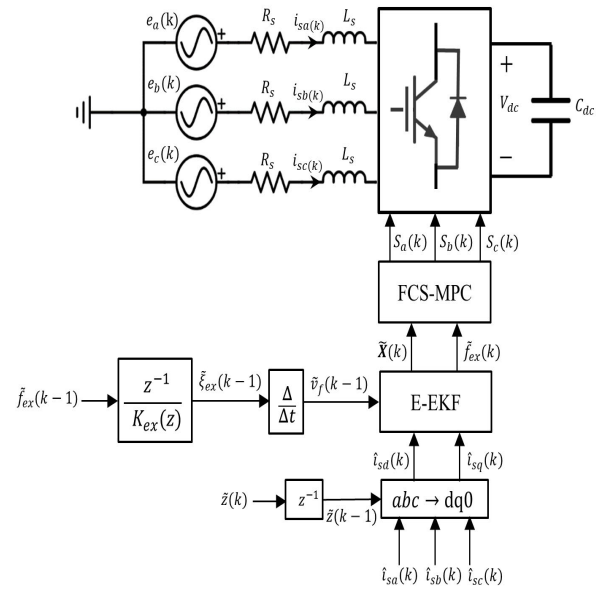


FIGURE 2. Schematic of the MSC and the proposed FCS-MPC strategy.

where

$$S_a(t) = \begin{cases} 1 & \text{if } S_1 \text{ is on and } S_4 \text{ is off} \\ 0 & \text{if } S_1 \text{ is off and } S_4 \text{ is on,} \end{cases}$$

$$S_b(t) = \begin{cases} 1 & \text{if } S_2 \text{ is on and } S_5 \text{ is off} \\ 0 & \text{if } S_2 \text{ is off and } S_5 \text{ is on,} \end{cases}$$

$$S_c(t) = \begin{cases} 1 & \text{if } S_3 \text{ is on and } S_6 \text{ is off} \\ 0 & \text{if } S_3 \text{ is off and } S_6 \text{ is on,} \end{cases}$$

Using the Park and Clarke transformation to transform the three-phase stator voltage vector $V_s(t)$ into its corresponding counterpart in the $d-q$ reference frame,

$$\begin{bmatrix} V_{sd}(t) \\ V_{sq}(t) \end{bmatrix} = K_{dq} \begin{bmatrix} V_{sa}(t) \\ V_{sb}(t) \\ V_{sc}(t) \end{bmatrix} \quad (4)$$

where

$$K_{dq} = \sqrt{\frac{2}{3}} \begin{bmatrix} \cos(\frac{\pi}{\gamma}z(t)) & -\sin(\frac{\pi}{\gamma}z(t)) \\ \cos(\frac{\pi}{\gamma}z(t) - \frac{2\pi}{3}) & -\sin(\frac{\pi}{\gamma}z(t) - \frac{2\pi}{3}) \\ \cos(\frac{\pi}{\gamma}z(t) + \frac{2\pi}{3}) & -\sin(\frac{\pi}{\gamma}z(t) + \frac{2\pi}{3}) \end{bmatrix}^T,$$

where $z(t)$ is the heave displacement of the oscillating body. By substituting (3) into (4), we obtain

$$\begin{bmatrix} V_{sd}(t) \\ V_{sq}(t) \end{bmatrix} = \frac{V_{dc}(t)}{3} K_{dq} K_s S(t). \quad (5)$$

B. WEC MECHANICAL SYSTEM MODEL

The forces acting on the WEC buoy oscillating in heave can be expressed using Newton's second law of motion as follows [20]

$$f_{ex}(t) - f_r(t) - f_b(t) - f_{rs}(t) - f_d(t) - f_f(t) - f_{em}(t) = m_b a(t), \quad (6)$$

where $f_{ex}(t)$, $f_r(t)$, $f_b(t)$, $f_{rs}(t)$, $f_d(t)$, $f_f(t)$, and $f_{em}(t)$ are the wave excitation, wave radiation, buoyancy, restoring, viscous drag, friction, and controlled electromagnetic forces, respectively. m_b and $a(t)$ are the mass of the oscillating body and the heave acceleration of the buoy, respectively. The heave acceleration of the WEC buoy can be represented as follows:

$$\begin{aligned}
a(t) = & \frac{1}{m_b + m_\infty} \left[f_{ex}(t) - \mathbf{C}_r \mathbf{q}(t) - \underbrace{S_{rs} z(t)}_{f_{rs}(t)} \right. \\
& - \underbrace{\pi \rho g R_b^2 \left(1 - \frac{|z(t)|z(t)}{3R_b^2} \right)}_{f_b(t)} z(t) \\
& - \underbrace{0.5 \rho A_w C_d |v(t) - v_f(t)| (v(t) - v_f(t))}_{f_d(t)} \\
& - \underbrace{F_n \left(\frac{\mu_v |v(t)|}{F_n} + \mu_d + (\mu_s - \mu_d) e^{-\left(\frac{|v(t)|}{v_s}\right)^2} \right)}_{f_f(t)} \text{sgn}(v(t)) \\
& \left. + \underbrace{\frac{3\pi \psi_{PM}}{2\gamma} i_{sq}(t)}_{f_{em}(t)} \right]. \quad (7)
\end{aligned}$$

The effect of the wave radiation force is represented as a linear time-invariant model of the form $\dot{\mathbf{q}}(t) = \mathbf{A}_r \mathbf{q}(t) + \mathbf{B}_r v(t)$, wherein $\mathbf{q}(t)$ represents the radiation auxiliary state vector and an output equation of $\mathbf{C}_r \mathbf{q}(t)$. The matrices \mathbf{A}_r , \mathbf{B}_r , and \mathbf{C}_r are the radiation state matrices. The parameters m_∞ , S_{rs} , and R_b are the added mass, restoring spring coefficient, and the buoy radius, respectively. The friction force between the moving parts of the WEC is represented as a Coulomb friction-force model exhibiting viscous and Stribeck effects; μ_v , μ_d , and μ_s are the viscous, dynamic, and static friction coefficients, respectively. F_n is the normal force, and $v_s(t)$ is the Stribeck velocity. The viscous drag force is represented as a quadratic function of the difference in the heave velocity between the buoy and the surrounding water surface, wherein ρ , A_w , C_d , and $v_f(t)$ are the sea water density, buoy submerged surface area, viscous drag coefficient, and water surface heave velocity, respectively [21].

C. WAVE-TO-WIRE WEC MODEL

The overall wave-to-wire nonlinear model of the WEC system can be concisely expressed in the continuous state space form as follows:

$$\begin{aligned}
\dot{x}_1(t) &= x_2(t), \quad (8) \\
\dot{x}_2(t) &= \frac{1}{m_b + m_\infty} \left[f_{ex}(t) - \mathbf{C}_r \mathbf{x}_3(t) - S_{rs} x_1(t) \right. \\
& - \pi \rho g R_b^2 \left(1 - \frac{|x_1(t)|x_1(t)}{3R_b^2} \right) x_1(t) \\
& - 0.5 \rho A_w C_d |x_2(t) - v_f(t)| (x_2(t) - v_f(t)) \\
& - \mu_v |x_2(t)| \text{sgn}(x_2(t)) - F_n \mu_d \text{sgn}(x_2(t)) \\
& - F_n (\mu_s - \mu_d) e^{-\left(\frac{|x_2(t)|}{v_s}\right)^2} \text{sgn}(x_2(t)) \\
& \left. + \frac{3\pi \psi_{PM}}{2\gamma} x_5(t) \right], \quad (9)
\end{aligned}$$

$$\dot{\mathbf{x}}_3(t) = \mathbf{A}_r \mathbf{x}_3(t) + \mathbf{B}_r x_2(t), \quad (10)$$

$$\dot{x}_4(t) = -\frac{u_1(t)}{L_s} - \frac{R_s}{L_s} x_4(t) + \frac{\pi}{\gamma} x_2(t) x_5(t), \quad (11)$$

$$\dot{x}_5(t) = -\frac{u_2(t)}{L_s} - \frac{R_s}{L_s} x_5(t) - \frac{\pi}{\gamma} x_2(t) x_4(t) - \frac{\pi \psi_{PM}}{\gamma} x_2(t), \quad (12)$$

$$\mathbf{y}(t) = \mathbf{x}(t), \quad (13)$$

where the state vector is $\mathbf{x}(t) = [x_1(t), x_2(t), \mathbf{x}_3(t), x_4(t), x_5(t)] = [z(t), v(t), \mathbf{q}(t), i_{sd}(t), i_{sq}(t)]$, the model input vectors are $u_1(t) = V_{sd}(t)$ and $u_2(t) = V_{sq}(t)$, and the output vector is $\mathbf{y}(t) = [x_1(t), x_2(t), \mathbf{x}_3(t), x_4(t), x_5(t)]$. The wave radiation effect is represented using a fourth-order linear time-invariant model $\mathbf{q}(t) \in \mathbb{R}^{4 \times 1}$. The corresponding state and output vectors are $\mathbf{x}(t), \mathbf{y}(t) \in \mathbb{R}^{8 \times 1}$.

III. WEC CONTROL STRATEGY

In this section, an estimator-based FCS-MPC strategy is developed for controlling the operation of the WEC. The control strategy aims to maximize the WEC-captured energy while limiting the PMLG stator current, consequently soft-constraining the physical limitations of the system.

A. MODEL DISCRETIZATION

Prior to discretizing the WEC model described in (8)–(13), the discontinuous friction model is replaced with a continuous and differentiable approximation of the following form [22]:

$$\begin{aligned}
f_f(t) \approx & -F_n \mu_d \tanh(\alpha v(t)) - \mu_v v(t) \\
& - F_n (\mu_s - \mu_d) e^{-\left(\frac{|v(t)|}{v_s}\right)^2} \tanh(\alpha v(t)). \quad (14)
\end{aligned}$$

The rate of change of the friction force is governed by the parameter α . The forward Euler method is implemented to transform the WEC nonlinear continuous-time model described in (8)–(13) into its discrete-time counterpart. This discrete-time model of the system can be conveniently represented in the compact state-space matrix form, wherein T_s would be the sampling time,

$$\mathbf{X}(k+1) = T_s [\mathbf{A}\mathbf{X}(k) + \mathbf{B}\mathbf{U}(k) + \mathbf{\Gamma}(k)], \quad (15)$$

$$\mathbf{Y}(k) = \mathbf{C}\mathbf{X}(k), \quad (16)$$

where

$$\begin{aligned}
\mathbf{X}(k+1) &= \begin{bmatrix} x_1(k+1) \\ x_2(k+1) \\ \vdots \\ x_5(k+1) \end{bmatrix}, \quad \mathbf{X}(k) = \begin{bmatrix} x_1(k) \\ x_2(k) \\ \vdots \\ x_5(k) \end{bmatrix}, \\
\mathbf{A} &= \begin{bmatrix} 0 & 1 & \mathbf{0}_{1 \times 4} & 0 & 0 \\ \frac{-S_{rs}}{m_b + m_\infty} & 0 & \frac{-\mathbf{C}_r}{m_b + m_\infty} & 0 & \frac{-3\pi \psi_{PM}}{2\gamma(m_b + m_\infty)} \\ \mathbf{0}_{4 \times 1} & \mathbf{B}_r & \mathbf{A}_r & \mathbf{0}_{4 \times 1} & \mathbf{0}_{4 \times 1} \\ 0 & 0 & \mathbf{0}_{1 \times 4} & \frac{-R_s}{L_s} & 0 \\ 0 & \frac{-\pi \psi_{PM}}{\gamma} & \mathbf{0}_{1 \times 4} & 0 & \frac{-R_s}{L_s} \end{bmatrix}, \\
\mathbf{B} &= \begin{bmatrix} 0 & 0 & \mathbf{0}_{1 \times 4} & -\frac{1}{L_s} & 0 \\ 0 & 0 & \mathbf{0}_{1 \times 4} & 0 & -\frac{1}{L_s} \end{bmatrix}^T,
\end{aligned}$$

TABLE 1. All possible combinations of switching states and their corresponding voltage vectors.

S_a	S_b	S_c	Voltage Vector \mathbf{V}
0	0	0	$\mathbf{V}_0 = 0$
1	0	0	$\mathbf{V}_1 = \frac{2}{3}V_{dc}$
1	1	0	$\mathbf{V}_2 = \frac{1}{3}V_{dc} + j\frac{\sqrt{3}}{3}V_{dc}$
0	1	0	$\mathbf{V}_3 = -\frac{1}{3}V_{dc} + j\frac{\sqrt{3}}{3}V_{dc}$
0	1	1	$\mathbf{V}_4 = -\frac{2}{3}V_{dc}$
0	0	1	$\mathbf{V}_5 = -\frac{1}{3}V_{dc} - j\frac{\sqrt{3}}{3}V_{dc}$
1	0	1	$\mathbf{V}_6 = \frac{1}{3}V_{dc} - j\frac{\sqrt{3}}{3}V_{dc}$
1	1	1	$\mathbf{V}_7 = 0$

$$\mathbf{C} = \begin{bmatrix} \mathbf{0}_{1 \times 6} & 1 & 0 \\ \mathbf{0}_{1 \times 6} & 0 & 1 \end{bmatrix},$$

$$\mathbf{\Gamma}(k) = [\mathbf{\Gamma}_1(k) \ \mathbf{\Gamma}_2(k) \ \mathbf{\Gamma}_3(k) \ \mathbf{\Gamma}_4(k) \ \mathbf{\Gamma}_5(k)]^T,$$

$$\begin{aligned} \mathbf{\Gamma}_1(k) = 0, \mathbf{\Gamma}_2(k) = & -\frac{1}{m_b + m_\infty} \left[-f_{ex}(k) \right. \\ & + \pi \rho g R_b^2 \left(1 - \frac{|x_1(k)|x_1(k)}{3R_b^2} \right) x_1(k) - \frac{3\pi \psi_{PM}}{2\gamma} x_5(k) \\ & + 0.5 \rho A_w C_d |x_2(k) - v_f(k)| (x_2(k) - v_f(k)) \\ & + F_n \mu_d \tanh(\alpha x_2(k)) + \mu_v x_2(k) \\ & \left. + F_n (\mu_s - \mu_d) e^{-\left(\frac{|x_2(k)|}{v_s}\right)^2} \tanh(\alpha x_2(k)) \right], \end{aligned}$$

$$\mathbf{\Gamma}_3(k) = \mathbf{0}_{4 \times 1}, \quad \mathbf{\Gamma}_4(k) = \frac{\pi}{\gamma} x_2(k) x_5(k),$$

$$\mathbf{\Gamma}_5(k) = -\frac{\pi}{\gamma} x_2(k) x_4(k), \quad \mathbf{U}(k) = \frac{V_{dc}(k)}{3} \mathbf{K}_{dq} \mathbf{K}_s \mathbf{S}(k).$$

B. PROPOSED REFERENCELESS FCS-MPC CONTROLLER

The proposed FCS-MPC approach does not require any desired reference signal. Instead, it is based on maximizing a cost function through an online search technique wherein the optimum switching state of the MSC is determined in real time. This is performed by predicting WEC system states one-sample ahead into the future. All possible eight switching combinations of 2L-VSC—shown in Table 1—are explored at every time instant k , and the switching state that maximizes a cost function is used to fire the 2L-VSC switches. One-sample-ahead prediction of the WEC system states is performed using the discrete model described in (15)-(16) and is expressed as follows:

$$\tilde{\mathbf{X}}(k + 1|k) = T_s [\mathbf{A}\tilde{\mathbf{X}}(k) + \mathbf{B}\mathbf{U}(k) + \tilde{\mathbf{\Gamma}}(k)], \quad (17)$$

$$\tilde{\mathbf{Y}}(k + 1|k) = \mathbf{C}\tilde{\mathbf{X}}(k + 1|k), \quad (18)$$

where the vectors $\tilde{\mathbf{X}}(k + 1|k)$ and $\tilde{\mathbf{Y}}(k + 1|k)$ represent the system state and output vectors predicted one sample ahead at $k + 1$, $\tilde{\mathbf{X}}(k)$ is the estimated system state vector at time instant k , and $\mathbf{U}(k)$ is the computed control vector at sampling instant k . The cost function, which is intended to be maximized, is the predicted WEC-converted (electrical)

energy $J(k + 1|k)$ at the terminals of the PMLG, that is

$$\max_{\mathbf{U}(k)} J(k + 1|k) = J(k) + \left[\frac{3T_s}{2} \tilde{\mathbf{Y}}(k + 1|k) \mathbf{U}(k) \right] \Theta(k), \quad (19)$$

where $J(k)$ is the converted energy at time instant k . The function $\Theta(k)$ is used to soft limit the quadrature component of the PMLG stator current $\tilde{x}_5(k + 1|k)$ and is expressed as follows [23]

$$\Theta(k) = \begin{cases} 1 & \text{if } -I_s^* \leq \tilde{x}_5(k + 1|k) \leq I_s^* \\ 1 \times 10^{-6} & \text{otherwise} \end{cases} \quad (20)$$

where I_s^* is the PMLG stator current constraint. I_s^* is calculated using the optimal flux weakening technique, wherein the PMLG electromagnetic force is maximized while restricting the machine stator current to its limit, which is calculated in real time as follows [24]:

$$I_s^* = \frac{\gamma}{\pi L_s \tilde{x}_2(k + 1|k)} \sqrt{V_s^{*2} - \left(\frac{\pi \tilde{x}_2(k + 1|k) \psi_{PM}}{\gamma} \right)^2}, \quad (21)$$

where V_s^* is the maximum phase voltage determined using the DC-link voltage V_{dc} and the deployed switching algorithm [24]. Herein, because the FCS-MPC technique is used, $V_s^* = 2V_{dc}/3$. To derive (21), the machine is assumed to be of a surface-mounted PMLG type, the machine stator currents are believed to have slow steady-state variations, and the direct-axis component of the stator current is believed to be significantly lower than the quadrature component [24]. Figure 3 depicts how I_s^* varies as function of the buoy heave velocity. Intuitively, as the buoy heave velocity increases, the PMLG stator current is further restricted. I_s^* primarily comprises the q-axis component of the stator current because $i_{sq}(k) \gg i_{sd}(k)$.

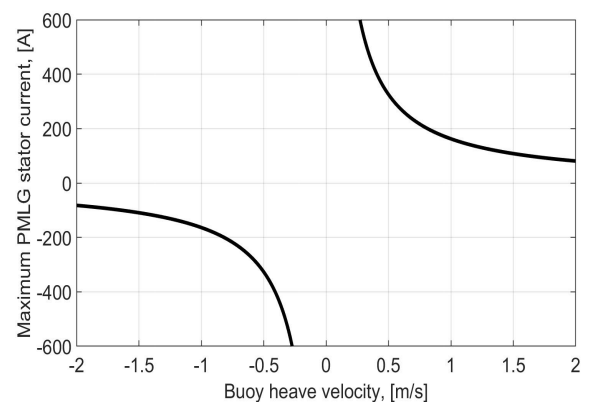


FIGURE 3. The maximum stator current limit I_s^* as a function of the WEC heave velocity $v(k)$.

The proposed referenceless FCS-MPC (RL-FCS-MPC) strategy is concisely described in the flowchart shown in Fig. 4. Only three-phase PMLG stator current measurements are required at every time instant k using current transducers, whereas no mechanical sensors (e.g., position and force sensors) are required.

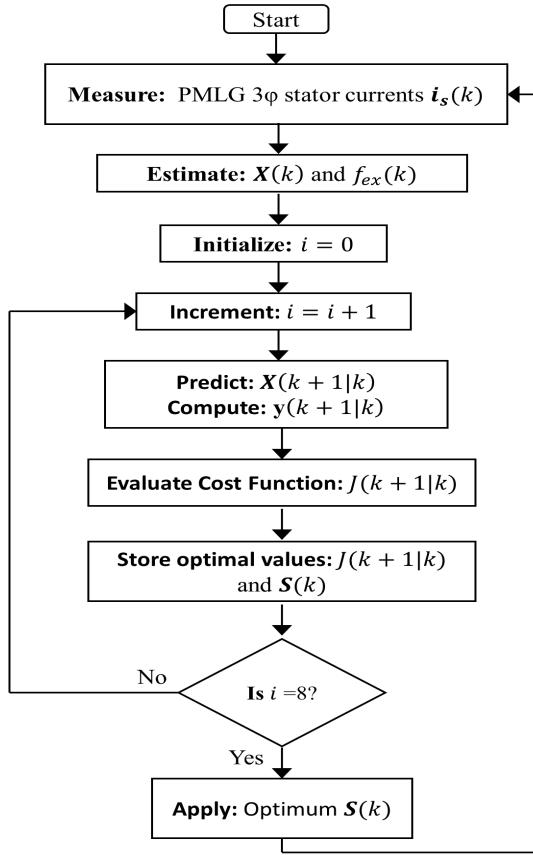


FIGURE 4. Flowchart of the proposed RL-FCS-MPC control strategy.

C. E-EKF ESTIMATOR

Similar to what was developed in [21], an electrical-based extended Kalman filter (E-EKF) is deployed to determine the system state vector $X(k)$ in (17). Furthermore, an E-EKF is used to estimate the wave excitation force $f_{ex}(k)$, which is represented as a random walk process, as follows:

$$f_{ex}(k) = f_{ex}(k-1) + T_s \epsilon(k-1), \quad (22)$$

where $\epsilon(k-1)$ is a random drift at time $k-1$ represented as white noise with zero mean and finite variance. Both estimated states are combined to form a new state vector $\zeta(k) = [\tilde{X}(k) \tilde{f}_{ex}(k)]^T$ and the WEC system model is represented in the following discrete nonlinear state-space model:

$$\zeta(k) = f(\zeta(k-1), \mathbf{u}(k-1), \mathbf{w}(k-1)), \quad (23)$$

$$\tilde{\mathbf{y}}(k) = \mathbf{g}(\zeta(k), \boldsymbol{\sigma}(k)), \quad (24)$$

where $f(\cdot)$ and $\mathbf{g}(\cdot)$ are the state and output (measurement) functions. The vector variables $\zeta(k-1)$, $\mathbf{u}(k-1)$, and $\mathbf{w}(k-1)$ are the estimated state, input, and process noise vectors, all evaluated at time instant $k-1$, respectively. The measurement function $\mathbf{g}(\cdot)$ arguments are the estimated state vector, $\zeta(k)$, and the measurement noise vector, $\boldsymbol{\sigma}(k)$, whereas $\tilde{\mathbf{y}}(k)$ is the estimated output vector. The state and measurement noise variables are represented as a white noise random variable with zero mean and known covariance matrices of $\mathbf{Q}(k)$ and $\mathbf{R}(k)$, respectively.

As shown in Fig. 2, the E-EKF estimator is fed the measured three-phase PMLG stator current. A one-sample-delayed estimate of the buoy displacement, $\tilde{z}(k-1)$, is used to transform the measured three-phase stator current signals into their corresponding $d-q$ rotating reference frame equivalents. The WEC system model described in (15) and (16) requires knowledge of the water surface velocity $v_f(k)$, which approximates the viscous drag force. The estimated wave excitation force is delayed by one sample and the wave elevation at $k-1$ is approximated using a 10th-order discrete wave-to-excitation force transfer function, $K_{ex}(z)$, that is consequently produced by solving the wave excitation problem in WAMIT [25]. The wave-to-excitation force discrete transfer function for the buoy design under study is expressed as follows:

$$K_{ex}(z) = \frac{a_0 + a_1z + a_2z^2 + \dots + a_{10}z^{10}}{b_0 + b_1z + b_2z^2 + \dots + b_{10}z^{10}}, \quad (25)$$

where the transfer function parameters are listed in Appendix A. Algorithm 1 summarizes the state estimation procedure at time instant k for the WEC system that uses an extended Kalman filter. This procedure is repeated at every sampling instant k .

Algorithm 1 Extended Kalman Filter

- (1) Initiate the estimated posteriori state vector $\tilde{\zeta}^+(k-1) = \mathbf{0} \in \mathbb{R}^{9 \times 1}$ and the posteriori estimation error covariance matrix $\mathbf{P}^+(k-1) = \mathbf{0} \in \mathbb{R}^{9 \times 9}$.
- (2) Calculate the Jacobian matrix evaluated at $\tilde{\zeta}^+(k-1)$:

$$\mathbf{F}(k-1) = \left. \frac{\partial f(k-1)}{\partial \zeta(k-1)} \right|_{\tilde{\zeta}^+(k-1)} \in \mathbb{R}^{9 \times 9}.$$

- (3) The time update equations:

$$\begin{aligned} &\text{The priori estimation error covariance matrix,} \\ &\mathbf{P}^-(k) = \mathbf{F}(k-1)\mathbf{P}^+(k-1)\mathbf{F}(k-1)^\top + \\ &\quad \mathbf{W}(k-1)\mathbf{Q}(k-1)\mathbf{W}(k-1)^\top \end{aligned}$$

$$\begin{aligned} &\text{The estimated priori state vector,} \\ &\tilde{\zeta}^-(k) = \mathbf{f}(\tilde{\zeta}^-(k-1), \mathbf{u}(k-1), \mathbf{0}), \end{aligned}$$

$$\begin{aligned} &\text{The process noise Jacobian matrix,} \\ &\mathbf{W}(k-1) = \frac{\partial f(k-1)}{\partial \mathbf{w}(k-1)} = T_s \mathbf{I}_{9 \times 9} \in \mathbb{R}^{9 \times 9}. \end{aligned}$$

- (4) The measurement update equations:

$$\begin{aligned} &\text{The Kalman filter gain at } k, \\ &\mathbf{K}(k) = \mathbf{P}^-(k)\mathbf{H}(k)^\top (\mathbf{H}(k)\mathbf{P}^-(k)\mathbf{H}(k)^\top + \\ &\quad \mathbf{D}(k)\mathbf{R}(k)\mathbf{D}(k)^\top)^{-1} \in \mathbb{R}^{9 \times 9}, \end{aligned}$$

$$\begin{aligned} &\text{The estimated posteriori state vector at } k, \\ &\tilde{\zeta}^+(k) = \tilde{\zeta}^-(k) + \mathbf{K}(k)[\mathbf{y}(k) - \mathbf{g}(\tilde{\zeta}^-(k), \mathbf{0})], \end{aligned}$$

$$\begin{aligned} &\text{The posteriori estimation error covariance matrix at } k, \\ &\mathbf{P}^+(k) = (\mathbf{I} - \mathbf{K}(k)\mathbf{H}(k))\mathbf{P}^-(k), \end{aligned}$$

$$\begin{aligned} &\text{The measurement equation Jacobian matrices,} \\ &\mathbf{H}(k) = \frac{\partial \mathbf{g}(k)}{\partial \zeta(k)} \in \mathbb{R}^{2 \times 9}, \mathbf{D}(k) = \frac{\partial \mathbf{g}(k)}{\partial \boldsymbol{\sigma}(k)} \in \mathbb{R}^{2 \times 9}. \end{aligned}$$

D. REFERENCE-BASED FCS-MPC CONTROLLER

The proposed RL-FCS-MPC strategy is compared to the benchmark resistive loading strategy. In the latter strategy,

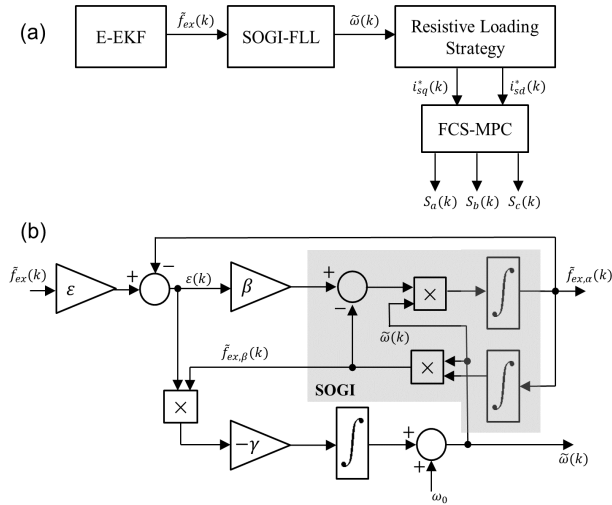


FIGURE 5. RB-FCS-MPC strategy with SOGI-FLL (a) general schematic diagram and (b) SOGI-FLL block diagram.

the desired (command) PTO electromagnetic force, $f_{em}^*(k)$, using the magnitude of the WEC intrinsic impedance, $Z_i(\omega)$, is derived as follows:

$$f_{em}^*(k) = -|Z_i(\omega)|v(k), \quad (26)$$

where

$$|Z_i(\omega)| = \sqrt{R_r(\omega)^2 + \left[\omega(m_b + M_r(\omega)) - \frac{(S_b + S_{rs})}{\omega} \right]^2},$$

where $R_r(\omega)$ and $M_r(\omega)$ are the WEC buoy radiation damping and radiation-added mass as a function of wave frequency ω , respectively. The parameter S_b is the buoy hydrostatic buoyancy stiffness coefficient [6]. The frequency-dependent hydrodynamic functions $R_r(\omega)$ and $M_r(\omega)$ are computed using hydrodynamic numerical tools, such as WAMIT. The resistive loading strategy requires real-time knowledge of the incident wave frequency, which is challenging to obtain considering the irregular nature of energetic sea environments. One way to overcome this problem is to preset the wave frequency at a fixed value representing the dominant (peak) wave frequency ω_p , resulting in a suboptimal energy absorption—that is only confined to the selected ω_p . Another approach—which is used herein—is to estimate the wave frequency in real time using the frequency estimation technique. Here, as shown in Fig. 4, the incident wave frequency is estimated using an adaptive bandpass filter through a second-order generalized integrator frequency-locked loop (SOGI-FLL). Recently, single phase FLL techniques have been gaining momentum in, particularly in power system applications, such as grid synchronization [26], flux estimation in AC drives [27], and in estimating electromechanical oscillations in power systems [28]. Herein, the SOGI-FLL estimates the instantaneous mechanical angular frequency, $\hat{\omega}(k)$, utilizing the estimated excitation force signal, $\hat{f}_{ex}(k)$, normalized by the coefficient ϵ , as shown in Fig. 5(a). As shown in Fig. 5(b), SOGI-FLL gains, namely,

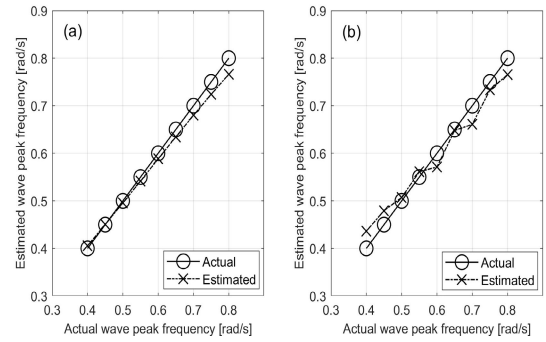


FIGURE 6. Developed SOGI-FLL frequency estimator performance (a) monochromatic sea states and (b) polychromatic sea states.

β and λ , are tuned as a trade-off between the frequency selectively and dynamic response of the SOGI-FLL [29]. Here, because the wave frequency range of interest is from 0.4 to 0.8 rad/s, the SOGI-FLL gains are set to $\beta = \sqrt{2}$ and $\lambda = 0.05$. The feedforward frequency, ω_o , is set to 0.6 rad/s, which is the midpoint frequency of the anticipated wave frequency range. The performance of the SOGI-FLL is assessed under monochromatic and polychromatic sea states with varying wave frequency, as shown in Fig. 6. For both types of sea states, the SOGI-FLL appropriately estimates the wave frequency with R^2 scores of 98.18% and 95.86% for monochromatic and polychromatic sea states, respectively. Here, the resistive loading strategy is implemented in a reference-based FCS-MPC (RB-FCS-MPC) framework in which the cost function to be minimized in this case, $E(k)$, is the error between the reference output vector, $Y^*(k)$, and the predicted output vector, $\tilde{Y}(k + 1|k)$, according to the following cost function:

$$\min_{U(k)} E(k) = \frac{\|Y^*(k) - \tilde{Y}(k + 1|k)\|^2}{\Theta(k)}, \quad (27)$$

where

$$Y^*(k) = [x_4^*(k), x_5^*(k)]^T, \\ \tilde{Y}(k + 1|k) = [\tilde{x}_4(k + 1|k), \tilde{x}_5(k + 1|k)]^T.$$

Similar to the algorithm presented in Fig. 4, at time instant k all eight possible switching functions, $S(k)$, are explored and the function that minimizes the cost function in (27) is implemented to fire the MSC switches. The function $\Theta(k)$ is deployed to limit the PMLG stator current. To minimize machine copper losses, the direct-axis component of the stator current command is set to zero, $x_4^*(k) = 0$. The quadrature-axis stator current command is represented as $x_5^*(k) = 2\gamma f_{em}^*(k)/3\pi\psi_{PM}$, where $f_{em}^*(k)$ is determined using (26).

IV. RESULTS AND DISCUSSION

To assess the performance of the developed control strategies, computer simulations are performed in MATLAB/Simulink. The WEC plant is modeled using the nonlinear state-space

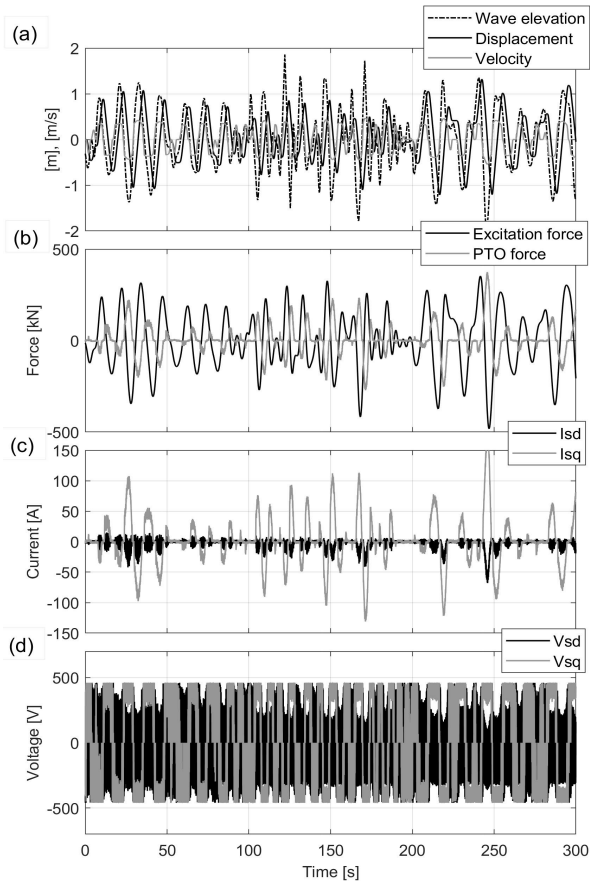


FIGURE 7. The mechanical and electrical dynamics of the WEC under the proposed RL-FCS-MPC strategy after the application of a 300 s long irregular sea state.

model described in (8)-(13). Polychromatic sea states are generated using the JONSWAP spectrum. The performance of the proposed RL-FCS-MPC strategy is compared to that of the RB-FCS-MPC strategy with SOGI-FLL. The parameters of the WEC model and control strategies are listed in Appendix A.

First, a polychromatic sea state is applied and the WEC mechanical and electrical performances under the RL-FCS-MPC strategy are observed. The sea state is made of three 100 s long irregular waves concatenated into a single 300 s long wave. The wave sequence characteristics are in the following order: $H_s = 2$ m and $T_p = 13$ s, $H_s = 4.75$ m and $T_p = 10$ s, and $H_s = 2.5$ m and $T_p = 14$ s. The resultant buoy motion dynamics, namely the heave displacement and velocity, are shown in Fig. 7 (a). The buoy excursions of the WEC are as high as the wave elevation for wave segments with large peak periods (i.e., $T_p = 13$ s and $T_p = 14$ s), whereas the heave velocity is regulated at 0.5 m/s. From Fig. 7 (b), the time-averaged PTO electromagnetic force under RL-FCS-MPC is approximately 46 kN, while the peak-to-average ratio of the PTO force is 7. The PMLG stator current $d-q$ components are plotted in Fig. 7 (c). The shape and magnitude of the stator current q component is observed to be correlated with the

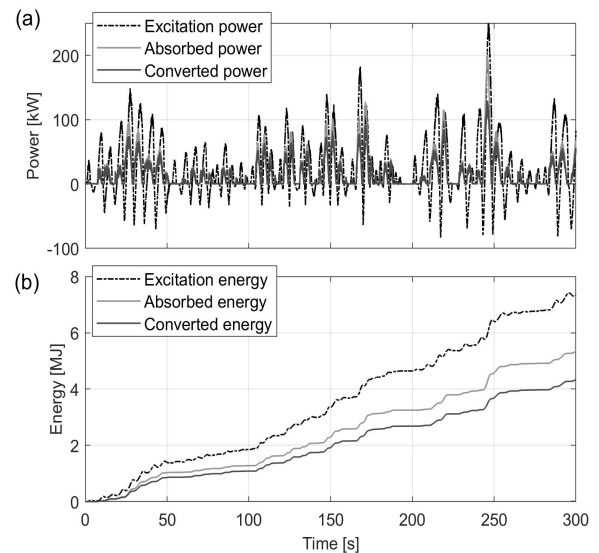


FIGURE 8. Resultant power and energy waveforms of the WEC under the proposed RL-FCS-MPC strategy subsequent to the application of a 300 s long irregular sea state.

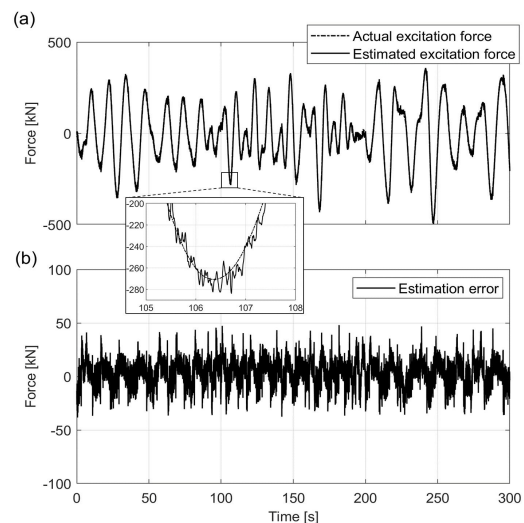


FIGURE 9. Performance of the E-EKF estimator in estimating the wave excitation force. (a) Actual and estimated excitation force waveforms and (b) the corresponding estimation error.

PTO force waveform. The control effort, namely, the switching function $S(k)$, is manifested in the $d-q$ components of the terminal stator voltage. The terminal stator voltage appears to be highly discontinuous, as depicted in Fig. 7 (d). Nevertheless, the stator voltage $d-q$ components are curtailed by the DC-link voltage V_{dc} , as $V_{sd}^2 + V_{sq}^2 \leq 2V_{dc}^2/3$. The instantaneous wave excitation power, which is the amount of power captured by the WEC buoy and is computed as $P_{ex}(k) = f_{ex}(k)v(k)$, is shown in Fig. 8 (a). The $P_{ex}(k)$ is bidirectional, which indicates that the RL-FCS-MPC is a suboptimal control strategy (i.e., $f_{ex}(k)$ and $v(k)$ are off-resonance). Conversely, the PTO instantaneous absorbed power, $P_{abs}(k)$, and the instantaneous converted power, $P_{comv}(k)$, are both unidirectional (shown in Fig. 8 (a)), indicating the damping

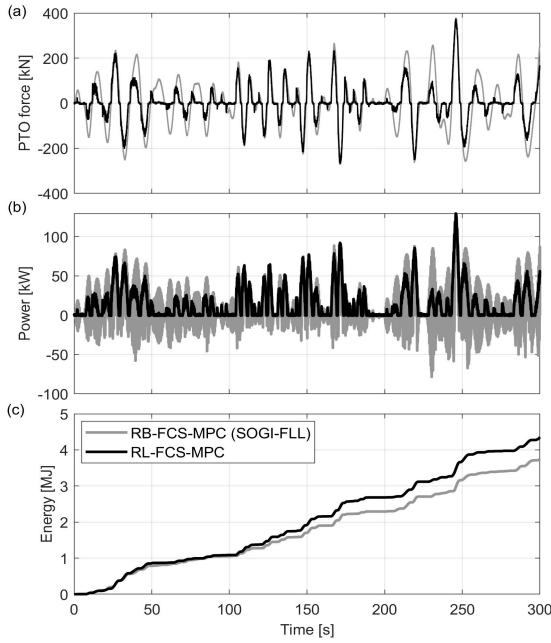


FIGURE 10. Performance comparison between the proposed RL-FCS-MPC strategy and the RB-FCS-MPC strategy: (a) PTO force, (b) instantaneous converted power, and (c) converted energy trajectories.

nature of the RL-FCS-MPC. The peak-to-average ratio of the WEC-converted power, P_{com}^*/\bar{P}_{com} , is 8.9, which is close to the values obtained when a resistive loading control strategy is applied. The absorbed power peak-to-average ratio, P_{abs}^*/\bar{P}_{abs} , is approximately 11, which is consistent with the ratio typically obtained using a resistive loading control strategy. Corresponding excitation, absorbed, and converted monotonic energy curves are depicted in Fig. 8 (b). The accumulated converted energy subsequent to a 300 s run of the system is approximately 4.35 MJ, corresponding to an overall mechanical-to-electrical conversion efficiency of 56 % and a PTO system conversion efficiency of approximately 80 %. The RL-FCS-MPC is fed with the estimated states using an electrical-based extended Kalman filter (E-EKF) and Fig. 9 demonstrates the goodness of the E-EKF estimator for estimating the wave excitation force, $f_{ex}(k)$. The root mean square error (RMSE) of the estimated $f_{ex}(k)$ is 12.5 kN. Furthermore, RMSE values for the estimated heave displacement and velocity are 0.011 m and 0.0042 m/s, respectively.

The effectiveness of the RL-FCS-MPC strategy is assessed against the RB-FCS-MPC strategy equipped with SOGI-FLL. As shown in Fig. 10 (a), the two control strategies used herein resulted in distinct PTO electromagnetic force waveforms. The WEC under the RL-FCS-MPC needed approximately 45% lower control effort compared with the RB-FCS-MPC. As for the converted power, Fig. 10 (b) suggests that $P_{com}(k)$ is bidirectional for RB-FCS-MPC. In other words, the real power flows back and forth between the PMLG and the DC-link capacitor, which is not the case with RL-FCS-MPC. Figure 10 (c) shows the amount of energy measured at the terminals of the PMLG and

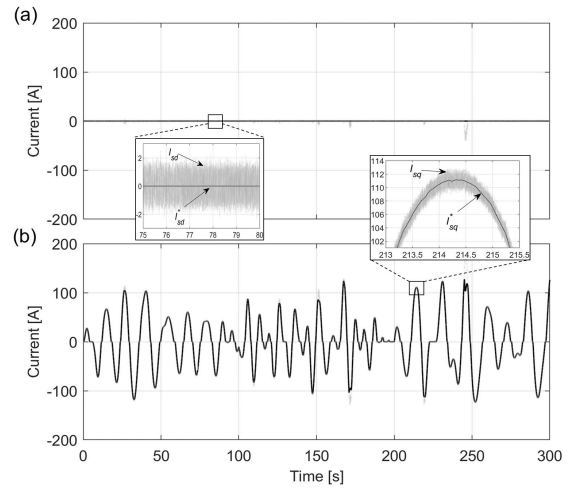


FIGURE 11. Tracking performance of the RB-FCS-MPC strategy (a) d -axis stator current component and (b) q -axis stator current component.

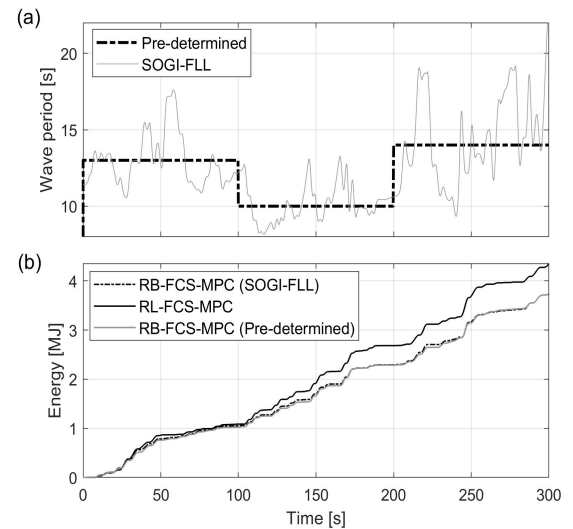


FIGURE 12. SOGI-FLL estimator performance: (a) estimation goodness and (b) resultant converted energy trajectories for the RB-FCS-MPC strategy with and without SOGI-FLL.

the RL-FCS-MPC clearly outperforms the RB-FCS-MPC by approximately 14%. The tracking performance of the RB-FCS-MPC is illustrated in Fig. 11. The measured d - q axis components of the PMLG stator current adequately follow the current reference trajectories with minimal steady-state errors. However, some ripples are observed owing to the deployment of the FCS-MPC. As discussed previously, the wave peak frequency is estimated online using the SOGI-FLL technique as part of the RB-FCS-MPC. As depicted in Fig. 12 (a), the SOGI-FLL technique properly estimated the wave peak frequency (or peak period) of the irregular 300 s long concatenated sea state. The instantaneous estimate of the wave peak period oscillates over the wave peak periods, which are known in advance ($T_p = 13, 10, 14$ s). This assessment is further evidenced by examining the accumulated

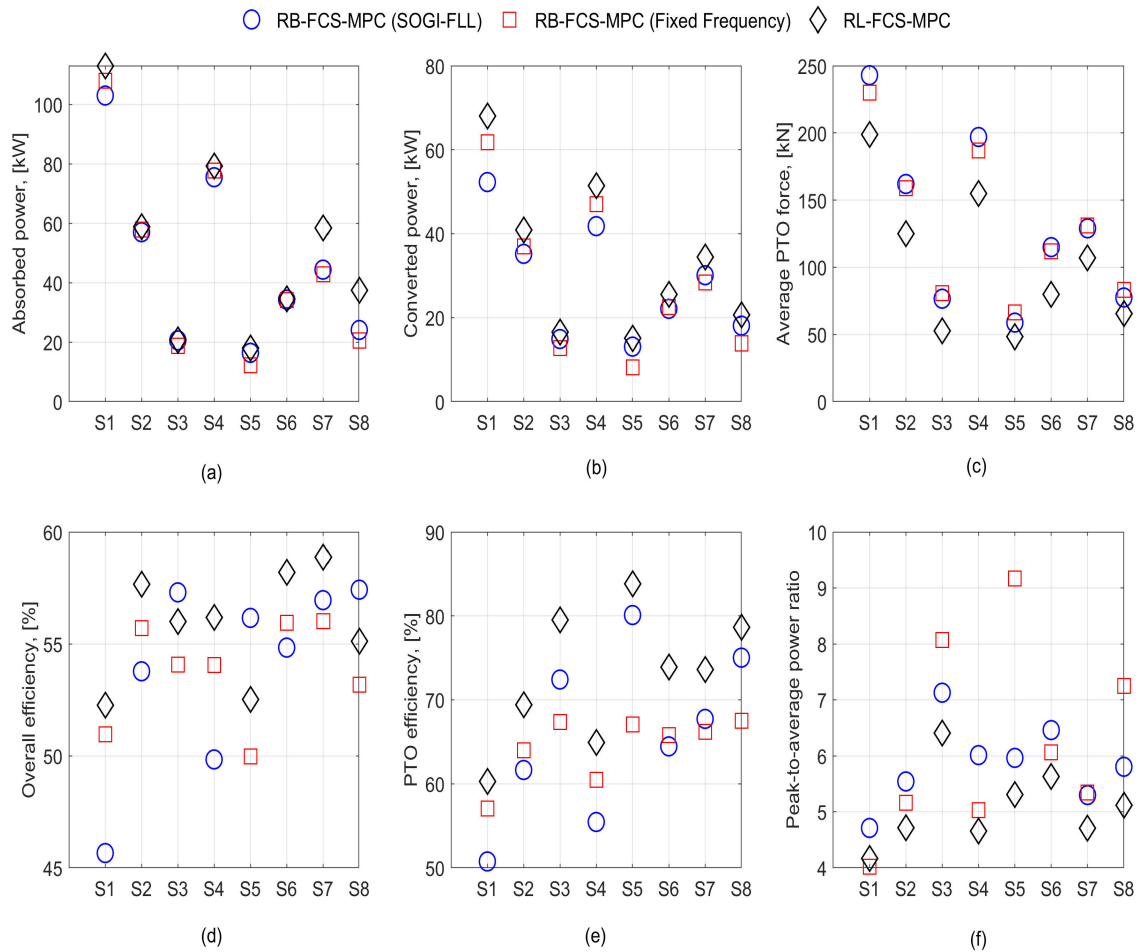


FIGURE 13. Comparison between RL-FCS-MPC, RB-FCS-MPC with SOGI-FLL, and RB-FCS-MPC with fixed frequency strategies under eight different polychromatic sea-states.

converted energy produced by the WEC under RB-FCS-MPC with SOGI-FLL and RB-FCS-MPC with manual modification of the wave peak period. With SOGI-FLL, the converted energy amounted to 3.747 MJ, whereas it was observed to be 3.761 MJ with manual alteration of the wave peak period. This clearly shows that the SOGI-FLL can properly estimating the wave peak period for a gradually changing sea environment.

Eight polychromatic sea states with varying peak periods, T_p , and significant height, H_s , are applied, and the performance of the different control strategies investigated herein is examined. Table 2 illustrates the characteristics of the applied sea states. In addition to the RL-FCS-MPC strategy and the RB-FCS-MPC strategy with SOGI-FLL, a simplified version of the RB-FCS-MPC strategy, wherein the wave frequency is kept unchanged and equal to the site dominant wave frequency, is also examined. As the wave peak periods of interest range from 8 s to 15 s, the RB-FCS-MPC with fixed wave frequency is tuned at a peak period of 12 s ($\omega_p = 0.52$ rad/s). As shown in Fig. 13, the three control strategies are compared with each other on

the basis of average mechanical absorbed power, \bar{P}_{abs} , average electrical converted power, \bar{P}_{conv} , average PTO electromagnetic force, \bar{f}_{em} , overall conversion efficiency, η_{ov} , PTO conversion efficiency, η_{pto} , and the peak-to-average ratio of the converted power, $P_{conv}^*/\bar{P}_{conv}$. The WEC under the RL-FCS-MPC absorbed more mechanical power, \bar{P}_{abs} , in all sea states than that absorbed in the other two strategies, as shown in Fig. 13 (a). The percentage increase in \bar{P}_{abs} of the RB-FCS-MPC compared with the SOGI-FLL and RB-FCS-MPC tuned at a fixed frequency ranges from 1% to 36% and 1% to 45%, respectively. Both reference-based strategies underperformed significantly for sea states with low peak periods (i.e., < 10 s). As for the average converted power, \bar{P}_{conv} , the RL-FCS-MPC produced 10% to 23% more power compared with the RB-FCS-MPC with SOGI-FLL, as shown in Fig. 13 (b). The RL-FCS-MPC required 18%–45% less electromagnetic force from the PTO system compared with the RB-FCS-MPC with SOGI-FLL and 15%–53% less PTO force compared with the RB-FCS-MPC tuned at a fixed frequency, as illustrated in Fig. 13 (c). The overall efficiency, η_{ov} , of the WEC under the RL-FCS-MPC varies between

TABLE 2. Applied polychromatic sea states generated using the JONSWAP spectrum.

Parameter (unit)	S1	S2	S3	S4	S5	S6	S7	S8
Significant height H_s (m)	4.75	3.75	3	4	2.75	3.5	4	3.75
Peak period T_p (s)	15	13	10	14	8	12	11	9

52% and 59%, which is close to that of an RB-FCS-MPC with fixed frequency, i.e., 50%–56%, as shown in Fig. 13 (d). This shows that the RL-FCS-MPC results in overall stable conversion efficiency values similar to those produced by the RB-FCS-MPC with a fixed frequency. Greater efficiency variations were recorded for the RB-FCS-MPC with SOGI-FLL, which is mainly attributed to instantaneous peak wave frequency alterations made by the SOGI-FLL. As for the PTO conversion efficiency, η_{pto} , the RL-FCS-MPC resulted in η_{pto} that ranges from 60% to 84% 13 (e). Lower η_{pto} values were recorded for energetic sea states (i.e., high T_p and H_s), which is intuitive considering that larger f_{em} is required, resulting in higher stator currents in the PMLG and hence greater copper losses in the machine. The opposite is true for less energetic sea states (i.e., low T_p and H_s). Despite managing to generate more power across all sea states compared to the other two control strategies, the RL-FCS-MPC produced the lowest converted power peak-to-average ratios, $P_{conv}^*/\bar{P}_{conv}$, ranging from 4.1 to 6.4, as illustrated in Fig. 13 (f). This indicates that the RL-FCS-MPC adequately utilizes PTO resources, facilitating the use of PTO systems with considerably low power ratings. Therefore, the initial capital investment required for the system is reduced.

V. CONCLUSION

Herein, an estimator-based predictive control strategy for controlling heaving WEC is proposed. The control strategy is based on an online search technique, wherein the optimum MSC switching functions are found at every time k . Therefore, no pre-determined reference trajectory is required. Due to the nonlinear nature of the FCS-MPC technique, a combined mechanical and electrical nonlinear model of the WEC is readily deployed, eliminating the need for splitting the control problem into two tiers. The proposed RL-FCS-MPC control strategy proved to be a practical damping control strategy, in which a noticeable increase in the converted energy is observed while utilizing lower PTO resources (i.e., lower $P_{conv}^*/\bar{P}_{conv}$ and lower f_{em}). The efficient use of PTO resources facilitates the use of PTO systems with low power ratings and, hence, reduces system costs. Despite the absence of an explicit hard-limiting mechanism to restrict the WEC buoy motion, the proposed control strategy resulted in modest buoy excursions that reduce the need for such hard constraints. E-EKF is utilized to eliminate the need for mechanical sensors and enhance the real-time implementation of the control strategy. The next step will be to address the problem of control strategy robustness against model uncertainties and un-modeled dynamics, which is a crucial

issue to wave energy. Moreover, experimental works are underway to further validate the developed control strategies.

**APPENDIX A
WEC DESIGN PARAMETERS**

A. MECHANICAL PARAMETERS

$T_s = 2 \times 10^{-4}$ s, $m_b = 57962$ kg, $\rho = 1025$ kg/m³, $A_w = 28.274$ m², $m_\infty = 28989$ kg, $R_b = 3$ m, $C_d = 1$.

$$A_r = \begin{pmatrix} -2.7936 & -5.9041 & -4.8634 & -2.8368 \\ 1 & 0 & 0 & 0 \\ 0 & 1 & 0 & 0 \\ 0 & 0 & 1 & 0 \end{pmatrix},$$

$$B_r = (1 \ 0 \ 0 \ 0)^T, \quad C_r = (43707 \ 64301 \ 57693 \ 0).$$

$a_0 = 4.337 \times 10^4$, $a_1 = -4.338 \times 10^5$, $a_2 = 1.952 \times 10^6$, $a_3 = -5.206 \times 10^6$, $a_4 = 9.11 \times 10^6$, $a_5 = -1.093 \times 10^7$, $a_6 = 9.111 \times 10^6$, $a_7 = -5.206 \times 10^6$, $a_8 = 1.953 \times 10^6$, $a_9 = -4.339 \times 10^5$, $a_{10} = 4.339 \times 10^4$, $b_0 = 0.9998$, $b_1 = -9.998$, $b_2 = 44.99$, $b_3 = -120$, $b_4 = 210$, $b_5 = -252$, $b_6 = 210$, $b_7 = -120$, $b_8 = 45$, $b_9 = -10$, $b_{10} = 1$.

$S_{rs} = 40000$ N/m, $F_n = 12000$ N, $\mu_d = 1$, $\mu_v = 2$, $\mu_s = 2$, $v_s = 1$ m/s, $\alpha = 10$, $V_{dc} = 690$.

$$R_r(\omega) = 30376\omega - 11248, \quad M_r(\omega) = -32801\omega^2 + 31430\omega + 42349,$$

B. PTO SYSTEM PARAMETERS

$R_s = 1.5$ Ω , $L_s = 35$ mH, $\psi_{PM} = 19.8$ Wb, $\gamma = 45$ mm.

C. E-EKF DESIGN PARAMETERS

$$Q = q' * q,$$

$$q = [1 \times 10^{-10}, 1 \times 10^{-10}, 2 \times 10^4, 1 \times 10^{-2}, 1 \times 10^{-2}],$$

$$R = \text{diag}(r),$$

$$r = [1 \times 10^{-3}, 1 \times 10^{-1}, 1 \times 10^{-2}].$$

REFERENCES

- [1] H. Chen, T. Tang, N. Ait-Ahmed, M. E. H. Benbouzid, M. Machmoum, and M. E.-H. Zaim, "Attraction, challenge and current status of marine current energy," *IEEE Access*, vol. 6, pp. 12665–12685, 2018.
- [2] Y. Zhu, X. Wang, Q. Ye, and C. Duan, "Comprehensive evaluation method for tidal current power generation device," *J. Modern Power Syst. Clean Energy*, vol. 4, no. 4, pp. 702–708, Oct. 2016.
- [3] X. He, W. He, Y. Liu, Y. Wang, G. Li, and Y. Wang, "Robust adaptive control of an offshore ocean thermal energy conversion system," *IEEE Trans. Syst., Man, Cybern. Syst.*, vol. 50, no. 12, pp. 5285–5295, Dec. 2020.
- [4] M. Ayob, V. Castellucci, and R. Waters, "Wave energy potential and 1–50 TWh scenarios for the Nordic synchronous grid," *Renew. Energy*, vol. 101, pp. 462–466, Feb. 2017.

- [5] A. Wahyudie and M. A. Jama, "Perspectives on damping strategy for heaving wave energy converters," *IEEE Access*, vol. 5, pp. 22224–22233, 2017.
- [6] J. Falnes, *Ocean Waves and Oscillating Systems*. Cambridge, U.K.: Cambridge Univ. Press, 2002.
- [7] A. de la Villa Jaén, A. García-Santana, and D. E. Montoya-Andrade, "Maximizing output power of linear generators for wave energy conversion," *Int. Trans. Electr. Energy Syst.*, vol. 24, no. 6, pp. 875–890, Jun. 2014.
- [8] J. Hals, J. Falnes, and T. Moan, "A comparison of selected strategies for adaptive control of wave energy converters," *J. Offshore Mech. Arctic Eng.*, vol. 133, no. 3, pp. 031101–031113, Aug. 2011.
- [9] F. Fusco and J. V. Ringwood, "A simple and effective real-time controller for wave energy converters," *IEEE Trans. Sustain. Energy*, vol. 4, no. 1, pp. 21–30, Jan. 2013.
- [10] A. Wahyudie, M. A. Jama, O. Saeed, H. Noura, A. Assi, and K. Harib, "Robust and low computational cost controller for improving captured power in heaving wave energy converters," *Renew. Energy*, vol. 82, pp. 114–124, Oct. 2015.
- [11] G. Li and M. Belmont, "Model predictive control of sea wave energy converters—Part I: A convex approach for the case of a single device," *Renew. Energy*, vol. 69, pp. 453–463, Sep. 2014.
- [12] M. Jama, A. Wahyudie, A. Assi, and H. Noura, "Controlling heaving wave energy converter using function-based model predictive control technique," in *Proc. 25th Chin. Control Decis. Conf. (CCDC)*, May 2013, pp. 2705–2710.
- [13] G. Bacelli and J. V. Ringwood, "Numerical optimal control of wave energy converters," *IEEE Trans. Sustain. Energy*, vol. 6, no. 2, pp. 294–302, Apr. 2015.
- [14] M. Jama, A. Assi, A. Wahyudie, and H. Noura, "Self-tunable fuzzy logic controller for the optimization of heaving wave energy converters," in *Proc. Int. Conf. Renew. Energy Res. Appl. (ICRERA)*, Nov. 2012, pp. 1–6.
- [15] P. Beirao, M. Mendes, D. Valerio, and J. Da Costa, "Control of the archimedes wave swing using neural networks," in *Proc. 7th Eur. Wave Tidal Energy Conf.*, Porto, Portugal, 2007, pp. 1–10.
- [16] X. Xiao, X. Huang, and Q. Kang, "A Hill-climbing-method-based maximum-power-point-tracking strategy for direct-drive wave energy converters," *IEEE Trans. Ind. Electron.*, vol. 63, no. 1, pp. 257–267, Jan. 2016.
- [17] E. A. Amon, T. K. A. Brekken, and A. A. Schacher, "Maximum power point tracking for ocean wave energy conversion," *IEEE Trans. Ind. Appl.*, vol. 48, no. 3, pp. 1079–1086, May 2012.
- [18] I. Boldea and S. Nasar, *Linear Electric Actuators and Generators*. Cambridge, U.K.: Cambridge Univ. Press, 1997.
- [19] P. Kou, D. Liang, J. Li, L. Gao, and Q. Ze, "Finite-control-set model predictive control for DFIG wind turbines," *IEEE Trans. Autom. Sci. Eng.*, vol. 15, no. 3, pp. 1004–1013, Jul. 2018.
- [20] M. Jama and A. Wahyudie, "Online damping strategy for controlling heaving wave energy converters using three-phase bridge boost rectifier," *IEEE Access*, vol. 5, pp. 7682–7691, 2017.
- [21] M. Jama, A. Wahyudie, and S. Mekhilef, "Wave excitation force estimation using an electrical-based extended Kalman filter for point absorber wave energy converters," *IEEE Access*, vol. 8, pp. 49823–49836, 2020.
- [22] S. Andersson, A. Söderberg, and S. Björklund, "Friction models for sliding dry, boundary and mixed lubricated contacts," *Tribol. Int.*, vol. 40, no. 4, pp. 580–587, Apr. 2007.
- [23] J. Rodriguez and P. Cortes, *Predictive Control of Power Converters and Electrical Drives*. West Sussex, U.K.: Wiley, 2012.
- [24] S. Sul, *Control of Electric Machine Drive Systems*. Hoboken, NJ, USA: Wiley, 2011.
- [25] WAMIT, Inc, Chestnut Hill, MA, USA. (2020). *WAMIT User Manual Version 7.4*. Accessed: Jun. 18, 2020. [Online]. Available: http://www.wamit.com/manualupdate/v74_manual.pdf
- [26] E. Oviedo, N. Vazquez, and R. Femat, "Synchronization technique of grid-connected power converters based on a limit cycle oscillator," *IEEE Trans. Ind. Electron.*, vol. 65, no. 1, pp. 709–717, Jan. 2018.
- [27] W. Xu, Y. Jiang, C. Mu, and F. Blaabjerg, "Improved nonlinear flux observer-based second-order SOFO for PMSM sensorless control," *IEEE Trans. Power Electron.*, vol. 34, no. 1, pp. 565–579, Jan. 2019.
- [28] M. Mansouri, M. Mojiri, M. A. Ghadiri-Modarres, and M. Karimi-Ghartemani, "Estimation of electromechanical oscillations from phasor measurements using second-order generalized integrator," *IEEE Trans. Instrum. Meas.*, vol. 64, no. 4, pp. 943–950, Apr. 2015.
- [29] A. M. Cantarellas, D. Remon, and P. Rodriguez, "Adaptive vector control of wave energy converters," *IEEE Trans. Ind. Appl.*, vol. 53, no. 3, pp. 2382–2391, May 2017.



MOHAMMED JAMA received the B.S. and Ph.D. degrees in electrical engineering from United Arab Emirates University, Al Ain, United Arab Emirates, in 2009 and 2015, respectively. From 2015 to 2018, he was a Postdoctoral Fellow with the Electrical Engineering Department, United Arab Emirates University, where he served as an Adjunct Faculty Member. He is currently a Research Fellow with the Emirates Centre of Energy and Environment Research (ECEER), United Arab Emirates University. His research interests include modeling and control of renewable energy systems, such as solar energy, wind energy, and marine energy, distributed generation, and energy storage systems.



BISNI FAHAD MON received the B.Tech. degree in applied electronics and instrumentation from Calicut University, India, in 2011, and the M.E. degree in embedded systems from Anna University, India, in 2014. She is currently pursuing the Ph.D. degree in electrical engineering from United Arab Emirates University, United Arab Emirates. From 2015, she was a Research Associate with the Department of Electrical Engineering, United Arab Emirates University. Her research interests include control of renewable energy systems and biomedical applications.



ADDY WAHYUDIE received the B.S. degree in electrical engineering from Gadjah Mada University, Indonesia, in 2002, with a focus on control systems, the M.Eng. degree in electrical engineering from Chulalongkorn University, Thailand, in 2005, and the D.Eng. degree in electrical engineering from Kyushu University, Japan, in 2010. From 2005 to 2011, he was a Lecturer with the Electrical Engineering Department, Gadjah Mada University. In 2011, he joined United Arab Emirates University, as an Assistant Professor. He is currently an Associate Professor with the Electrical Engineering Department, United Arab Emirates University. His research interests include control systems theory, such as robust control, intelligent control, and model predictive control, and its application in electromechanical and renewable energy systems (marine energy).



SAAD MEKHILEF (Senior Member, IEEE) received the B.Eng. degree in electrical engineering from the University of Sétif, Sétif, Algeria, in 1995, and the master's degree in engineering science and the Ph.D. degree in electrical engineering from the University of Malaya, Kuala Lumpur, Malaysia, in 1998 and 2003, respectively. He is currently a Professor and the Director of the Power Electronics and Renewable Energy Research Laboratory, Department of Electrical Engineering, University of Malaya. He is also the Dean of the Faculty of Engineering, University of Malaya. He is also a Distinguished Adjunct Professor with the School of Software and Electrical Engineering, Faculty of Science, Engineering and Technology, Swinburne University of Technology, Melbourne, Australia. He has authored or coauthored more than 450 publications in international journals and conference proceedings. His current research interests include power converter topologies, control of power converters, renewable energy, and energy efficiency.